



1 **A Numerical Study of Near Inertial Motions in Mid-Atlantic Bight**
2 **Area Induced by Hurricane Irene (2011)**

3 Peida Han¹ and Xiping Yu²

4 **Abstract**

5 Hurricane Irene generated strong near inertial currents (NICs) in the ocean waters when
6 passing over the Mid-Atlantic Bight (MAB) of the U. S. East Coast in late August 2011. It
7 is demonstrated that a combination of the valuable field data with detailed model results can
8 be exploited to study the development and decay mechanism of this event. Numerical results
9 obtained with regional oceanic modeling system (ROMS) are shown to agree well with the
10 field data. Both computed and observed results show that the NICs were significant in most
11 areas of the MAB region except in the nearshore area where the stratification was totally
12 destroyed by the hurricane-induced strong mixing. Based on the energy budget, it is clarified
13 that the near inertial kinetic energy (NIKE) was mainly gained from the wind power during
14 the hurricane event. In the deep water region, NIKE was basically balanced by the vertical
15 turbulence diffusion (40%) and downward divergence (33%). While in the continental shelf
16 region, NIKE was mainly dissipated by the vertical turbulence diffusion (67%) and partially
17 by the bottom friction (24%). Local dissipation of NIKE due to turbulence diffusion is much
18 more closely related to the rate of the vertical shear rather than the intensity of turbulence.
19 The strong vertical shear at the offshore side of the continental shelf led to a rapid
20 dissipation of NIKE in this region.

21 **Keywords:** Hurricane Irene; Mid-Atlantic Bight; Near inertial current; Energy budget;
22 Timescale of near inertial energy decay

¹ PhD Candidate. Department of Hydraulic Engineering, Tsinghua University, Beijing, China.

² Corresponding Author. Professor. Department of Ocean Science and Engineering, Southern
University of Science and Technology, Shenzhen, China. Email: yuxp@sustech.edu.cn



23 **1. Introduction**

24 Near inertial currents (NICs), observed widely in ocean basins around the world, are
25 characterized by the important role of Coriolis effect and by the periodic motion with the
26 frequency of an inertial mode (Garrett, 2001). The basic energy source of these freely
27 flowing currents is the wind power (Pollard, 1980; D'Asaro et al., 1985). Globally, the
28 annually averaged wind power supply to NICs was estimated ranging from 0.3 TW to more
29 than 1 TW by previous investigators (Alford, 2003a; Furuichi et al., 2008; Rimac et al.,
30 2013). As a comparison, the total power required to maintain the abyssal stratification and
31 the thermohaline circulation is about 2 TW (Munk and Wunsch, 1998). This implies that
32 NIC is a very important phenomenon in physical oceanography. In fact, NICs are believed
33 to have a significant role in upper-ocean mixing, which may substantially affect the
34 thermohaline circulation and even modulate the climate (Gregg, 1987; Alford, 2003b;
35 Jochum et al., 2013).

36 A tropical or an extratropical cyclone (hereinafter collectively referred as TC) is a
37 rotating low-pressure and strong-wind mesoscale weather system, which generates NICs
38 more powerfully than other types of atmospheric processes in nature (Alford et al., 2016;
39 Steiner et al., 2017). When a TC passes over a deep ocean, enormous energy is directly
40 transferred into the ocean waters, which rapidly generates strong NICs with a velocity up to
41 1 m/s in the horizontal direction of the mixed layer (Price, 1983; Sanford et al., 2011). Right-
42 bias effect is often shown in the NIC pattern, i.e., NICs are more intense on the right side of
43 the hurricane track, due to the resonance between the surface flow driven by NICs and
44 clockwise rotating wind stress on the right side (Chang and Anthes, 1978; Price, 1994).
45 After the passage of a TC, the surface near inertial energy usually persists for several inertial
46 cycles, and then gradually decays (Price, 1983; Sanford et al., 2011; Hormann et al., 2014;
47 Zhang et al., 2016; Wu et al., 2020).

48 It is known that NICs in shallow waters show some significant differences with those
49 in deep waters and the velocity of NICs in shallow waters is usually of a smaller magnitude
50 of 0.1-0.5 m/s (Chen and Xie, 1997; Rayson et al., 2015; Yang et al., 2015; Chen et al., 2017;



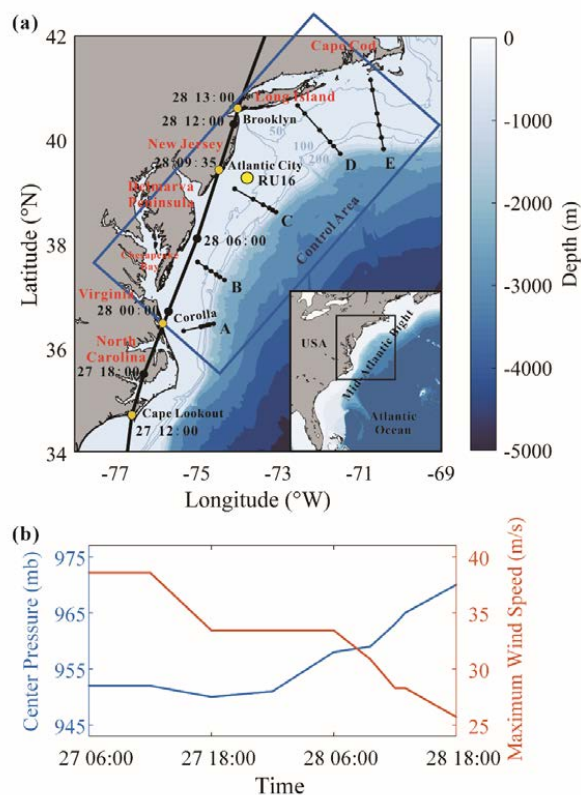
51 Zhang et al., 2018). The decrease of current velocity in shallow waters may be an effect of
52 the sea-bottom friction as Rayson et al. (2015) pointed out. Chen and Xie (1997), however,
53 found that it was because a significant part of the wind input, which may otherwise be an
54 energy source of the NICs, was exhausted to generate a wave-induced nearshore current
55 system. Chen et al. (2017) considered that barotropic waves in the shallow waters, such as
56 seiches, may trap some wind energy. In addition to the difference in magnitude, the modes
57 of the NICs in shallow and deep waters are also different. More specifically, a two-layer
58 structure was observed in shallow waters in several studies, i.e., NICs were in opposite
59 phases in surface and bottom layers, which differed from the conventional multi-layer mode
60 in deep waters (Chen et al., 1996; Shearman, 2005; Yang et al., 2015), though a multi-layer
61 mode may also be observed sometimes in nearshore waters due to combined effect of
62 changing wind stress, variable stratification and nonlinear bottom friction (Mackinnon and
63 Gregg, 2005).

64 There have been a considerable number of studies on the decay of specific TC
65 generated NICs in coastal regions. Rayson et al. (2015) paid attention to four intense TCs
66 on the Australian North-West Shelf and related the rapid decay of NICs in shallow waters
67 to the bottom friction. Yang et al. (2015) examined coastal ocean responses to Typhoon
68 Washi and found that the negative background vorticity could trap near inertial energy and
69 result in a slow decay. Shen et al. (2017) investigated five TCs over the Taiwan Strait and
70 identified a rapid decaying rate due to nonlinear interaction between NICs and tides. Zhang
71 et al. (2018) studied Hurricane Arthur in Mid-Atlantic Bight and showed that excessive wind
72 input does not necessarily lead to amplification of NICs because intensive wind input is
73 usually accompanied by an even higher rate of energy dissipation.

74 Though a significant number of investigations have been conducted, some basic
75 features of a TC induced NIC in the coastal ocean are still not clarified. For instance, the
76 energy budget in the NIC generated by a TC has not yet been thoroughly discussed in either
77 deep or shallow waters; and the relative importance of different physical processes including
78 advection, conversion, turbulence diffusion, bottom friction, energy divergence, etc., in the



79 energy budget has not yet been fully understood. In addition, it is still not concluded on
80 which processes dominate the decay of near inertial energy or on how each physical process
81 affects the decay rate of the near inertial energy in deep and shallow waters, respectively.
82 Our limited understanding to the basic features of a TC induced NIC is largely due to the
83 difficulties in ocean observations under extreme weather.
84



85

86 Figure 1. (a) Map of the MAB region. Best track of Hurricane Irene (2011) reported by Avila
87 and Cangialosi (2011) is shown by a black line. Reanalysis data provided by H*WIND
88 shows a similar track with Avila and Cangialosi (2011) and is thus omitted. The mean
89 position of Glider RU16 is marked by a yellow circle. Five virtual sections defined in
90 Section 3 are marked by short black lines. The control domain defined in Section 4 is marked
91 by a blue box. (b) Time series of center pressure and 10-m maximum wind speed of
92 Hurricane Irene reported by Avila and Cangialosi (2011).

93



94 In this study, we pay a close attention to the NIC induced by Hurricane Irene (2011).
95 Hurricane Irene (2011) crossed over the Mid-Atlantic Bight (MAB), a coastal region of the
96 North Atlantic, extending from Cape Cod, Massachusetts to Cape Lookout, North Caroline,
97 USA, as shown in Figure 1a. Before the hurricane event, seawater stratification in MAB
98 was quite strong due to the Cold Pool effect (Lentz, 2017) and the temperature difference
99 between the surface and the bottom exceeded 10 °C. During the passage of Hurricane Irene
100 (2011), a network of High-frequency (HF) radars measured the surface currents in MAB
101 (Roarty et al., 2010). Meanwhile, a Slocum glider launched near New Jersey measured the
102 vertical profiles of the temperature and the salinity (Schofield et al., 2010). Combination of
103 the valuable field data with effective numerical techniques then provided an opportunity to
104 achieve a comprehensive study of the NICs generated by this hurricane event.

105 2. Numerical Model

106 2.1 Basic Equations

107 In this study, the ocean responses to Hurricane Irene (2011) are studied using the
108 regional oceanic modeling system (ROMS) (Shchepetkin and McWilliams, 2005;
109 Haidvogel et al., 2008). ROMS deals with the Reynolds-averaged N-S equations in the σ
110 coordinate system (Freeman et al., 1972). Specifically, the Cartesian coordinate z is
111 replaced by σ based on a general relation $\chi(\sigma) = (z - \eta) / D$, where η is the vertical
112 displacement of the free surface and D is the instantaneous water depth, while $\chi(\sigma)$ is
113 a stretching function introduced for grid refinement. In the σ -coordinate system the
114 Reynolds-averaged N-S equations may finally be expressed as

$$115 \quad \frac{\partial \xi}{\partial t} + \frac{\partial(\xi u)}{\partial x} + \frac{\partial(\xi v)}{\partial y} + \frac{\partial(\xi \omega)}{\partial \sigma} = 0 \quad (1)$$

$$116 \quad \begin{aligned} & \frac{\partial(\xi u)}{\partial t} + \frac{\partial(\xi uu)}{\partial x} + \frac{\partial(\xi uv)}{\partial y} + \frac{\partial(\xi u \omega)}{\partial \sigma} - f \xi v + \frac{\xi}{\rho} \frac{\partial p}{\partial x} \\ & = -g \xi \left(\chi \frac{\partial D}{\partial x} + \frac{\partial \eta}{\partial x} \right) + \frac{\partial}{\partial \sigma} \left(\frac{\nu}{\xi} \frac{\partial u}{\partial \sigma} \right) + \frac{\partial}{\partial x} \left(\xi \nu' \frac{\partial u}{\partial x} \right) + \frac{\partial}{\partial y} \left(\xi \nu' \frac{\partial u}{\partial y} \right) \end{aligned} \quad (2)$$



$$\begin{aligned}
 & \frac{\partial(\xi v)}{\partial t} + \frac{\partial(\xi uv)}{\partial x} + \frac{\partial(\xi v v)}{\partial y} + \frac{\partial(\xi v \omega)}{\partial \sigma} + f \xi u + \frac{\xi}{\rho} \frac{\partial p}{\partial y} \\
 & = -g \xi \left(\chi \frac{\partial D}{\partial y} + \frac{\partial \eta}{\partial y} \right) + \frac{\partial}{\partial \sigma} \left(\frac{\nu}{\xi} \frac{\partial v}{\partial \sigma} \right) + \frac{\partial}{\partial x} \left(\xi \nu' \frac{\partial v}{\partial x} \right) + \frac{\partial}{\partial y} \left(\xi \nu' \frac{\partial v}{\partial y} \right)
 \end{aligned} \tag{3}$$

$$0 = -\frac{1}{\rho} \frac{\partial p}{\partial \sigma} - g \xi \tag{4}$$

$$\begin{aligned}
 & \frac{\partial(\xi C)}{\partial t} + \frac{\partial(\xi u C)}{\partial x} + \frac{\partial(\xi v C)}{\partial y} + \frac{\partial(\xi \omega C)}{\partial \sigma} \\
 & = \frac{\partial}{\partial \sigma} \left(\frac{\kappa}{\xi} \frac{\partial C}{\partial \sigma} \right) + \frac{\partial}{\partial x} \left(\xi \kappa' \frac{\partial C}{\partial x} \right) + \frac{\partial}{\partial y} \left(\xi \kappa' \frac{\partial C}{\partial y} \right)
 \end{aligned} \tag{5}$$

120 where, $\xi = \partial z / \partial \sigma = D(\partial \chi / \partial \sigma)$; u , v , ω are the velocity components in x , y , σ
 121 directions, respectively; C stands for the potential temperature T or salinity S ; p is
 122 the seawater pressure; ρ is the density of the seawater; $f = 2\Omega \sin \phi$ is the Coriolis
 123 parameter with $2\Omega = 1.458 \times 10^{-4} \text{ s}^{-1}$ and ϕ being the latitude; ν and κ are the
 124 diffusion coefficients for momentum and potential temperature or salinity, respectively, in
 125 the vertical direction; ν' and κ' are those in the horizontal directions; Note that Eq. (1)
 126 is the continuity equation; Eqs. (2) and (3) are equations of motion in two horizontal
 127 directions; Eq. (4) is the hydrostatic assumption; Eq. (5) is the advection-diffusion equation
 128 of the potential temperature or the salinity. The density of the seawater ρ is determined
 129 following the equation of state proposed by Jackett and McDougall (1995):

$$\rho(S, T, p) = \frac{\rho_0}{1 - p/K(S, T, p)} \tag{6}$$

131 where $\rho_0 = \rho(S, T, 0)$ is the seawater density at the standard atmospheric pressure and
 132 $K(S, T, p)$ is the bulk modulus, both are given by Jackett and McDougall (1995).

133 The vertical mixing is known to play an important role in determining the structure of
 134 a NIC, so it must be properly evaluated. In this study, we consider $\nu = \nu_0 + \nu_e$ and
 135 $\kappa = \kappa_0 + \kappa_e$, in which ν_0 and κ_0 are the molecular viscosity and diffusivity of the
 136 seawater, set to $\nu_0 = 10^{-5} \text{ m}^2/\text{s}$ and $\kappa_0 = 10^{-6} \text{ m}^2/\text{s}$ following previous suggestions (Xu
 137 et al., 2002; Li and Zhong, 2007; Lentz, 2017), while ν_e and κ_e are the eddy viscosity
 138 and diffusivity, determined by the conventional k- ϵ turbulence model (see Rodi (1987) and



139 Umlauf and Burchard (2003) for detailed description), a widely employed model that
140 demonstrated good performance in simulating various oceanographic processes
141 (Olabarrieta et al., 2011; Toffoli et al., 2012; Zhang et al., 2018).

142 Horizontal mixing is included in Eqs. (2), (3) and (5), though it has been pointed out
143 to play a relatively insignificant role in simulating response of the stratified ocean to a
144 hurricane, as compared to vertical mixing (Li and Zhong, 2007; Zhai et al., 2009; Dorostkar
145 et al., 2010). In the ocean basin of the present interest, the horizontal diffusion coefficient
146 was estimated to be an order of $10 \text{ m}^2/\text{s}$ under extreme conditions, e.g., TC condition
147 (Allahdadi, 2014; Mulligan and Hanson, 2016). Thus, we take $\nu' = \kappa' = 10 \text{ m}^2/\text{s}$ in the
148 present study for simplicity to simulate the ocean response to Hurricane Irene.

149 2.2 Computational Conditions

150 In order to fully capture the NIC induced by Hurricane Irene (2011), our computational
151 domain covers the entire MAB regions of the U. S. East Coast extending from Cape Cod,
152 Massachusetts, to Cape Lookout, North Caroline. The computational domain is discretized
153 into 35 layers with refinement near the surface and covered with a $5 \text{ km} \times 5 \text{ km}$ grid in the
154 horizontal plane. The 1 arc-min bathymetry data is obtained from ETOPO1 Global Relief
155 Model (Amante and Eakins, 2009) and resampled to a resolution of 5 km. The simulation
156 starts from 20 August, one week before the hurricane event and lasted for a period of 16
157 days. The time step is set to 1 min.

158 The initial and open boundary conditions of the seawater temperature and salinity, the
159 ocean flow velocities and the sea surface elevation are all from the Hybrid Coordinate Ocean
160 Model (HYCOM, <https://www.hycom.org/>) with a resolution of $1/12^\circ$ in space and 3 hr in
161 time (Cummings, 2005; Chassignet et al., 2007). The initial stratification in the HYCOM is
162 examined through a comparison with the 4D data provided by Experimental System for
163 Predicting Shelf and Slope Optics (ESPreSSO, <http://www.myroms.org/espresso/>). Seven
164 tidal constituents (M2, S2, N2, K2, O1, K1, Q1) included in the simulation are derived from
165 the ADvanced CIRCulation model (ADCIRC, <https://adcirc.org/>). Daily inflows from the
166 eleven largest rivers, containing Susquehanna River, Delaware River, Hudson River,



167 Potomac River, etc., are obtained from the United States Geological Survey (USGS,
168 <https://waterdata.usgs.gov/>). The so-called radiation-nudging condition is adopted at the
169 open boundaries (Marchesiello et al., 2001). Wet-and-dry option is activated at coastal
170 boundaries (Warner et al., 2013). The seabed boundary condition is required to satisfy:

$$171 \quad \nu \frac{\partial \mathbf{u}}{\partial z} = \tau_b = \rho \left[\frac{\lambda}{\ln(\Delta z / z_0)} \right]^2 |\mathbf{u}_b| \mathbf{u}_b \quad (7)$$

172 where, τ_b is the bottom friction; λ is the von Karman constant; \mathbf{u}_b is the fluid velocity
173 at the center of the bottom layer; Δz is the distance between the center of the bottom layer
174 and the seabed; z_0 is the bottom roughness, which is set to 0.02 m in MAB following
175 Churchill et al. (1994).

176 The hurricane wind forcing required in this study can be obtained from two sources,
177 i.e., the H*WIND data, with a spatial resolution of 6 km and a temporal resolution of 6 hr,
178 published by Atlantic Oceanographic and Meteorological Laboratory, National Oceanic and
179 Atmospheric Administration (AOML/NOAA) (https://www.aoml.noaa.gov/hrd/data_sub/wind.html) (Powell et al., 1998) and the North American Mesoscale (NAM) data, with a
180 spatial resolution of 12 km and a temporal resolution of 3 hr, provided by National Centers
181 for Environmental Prediction (NCEP) (<https://www.ncdc.noaa.gov/data-access/model-data/model-datasets/north-american-mesoscale-forecast-system-nam>) (Janjic et al., 2004).
182 In our computation, the former is used between 26 and 31 August (during the hurricane
183 event) because it has a better accuracy in capturing the maximum wind speed, while the
184 latter is used during other periods of the simulation. Reanalysis data for other atmospheric
185 forcing, such as the surface air temperature, air pressure, relative humidity, radiation and
186 precipitation are also available from NAM for determining the surface buoyancy fluxes. In
187 particular, the momentum flux τ_s can be estimated through (Fairall et al., 1996):

$$190 \quad \tau_s = \rho_a C_d u_{10}^2 \quad (8)$$

191 where, ρ_a is the density of the air; C_d is the coefficient for momentum; u_{10} is the
192 horizontal wind speed at the 10-m level; Several studies have confirmed that C_d does not



193 increase but level off or even decrease at high wind speeds (Emanuel, 1995; Powell et al.,
 194 2003; Donelan et al., 2004). Besides, C_d could be altered due to wave deformation in
 195 response to bathymetry change, especially in coastal regions (Chen et al., 2018; Xu and Yu,
 196 2021). Therefore, we choose a well verified formula based on the numerical results from
 197 the improved wave boundary layer model presented by Chen and Yu (2016), Chen et al.
 198 (2018) and Xu and Yu (2021), which considered the effects of both bathymetry and wind
 199 speed to determine C_d :

$$200 \quad C_d = C_{dw} + \frac{C_{d0} - C_{dw}}{(W_0 - W)^2} (u_{10} - W)^2 \quad (9)$$

201 where C_{d0} is a threshold value set to 0.001 for the wind stress at $u_{10} \leq W_0 = 5$ m/s, C_{dw}
 202 is the saturated wind stress coefficient and W is the saturation wind speed. We have

$$203 \quad C_{dw} = \begin{cases} -1.86 \times 10^{-4} \ln \frac{gD}{W_D} + 0.0025 & \frac{gD}{W_D} \leq 3 \\ 0.00225 & \frac{gD}{W_D} > 3 \end{cases} \quad (10)$$

$$204 \quad W = \begin{cases} 4.64 \ln \left(\frac{gD}{W_D} \right) + 42.6 & \frac{gD}{W_D} \leq 0.6 \\ W_D & \frac{gD}{W_D} > 0.6 \end{cases} \quad (11)$$

205 where W_D set to 40 m/s is the saturation wind speed in deep water. Except for the
 206 momentum flux, other air-sea fluxes, e.g., the sensible heat flux and the latent heat flux, are
 207 determined based on the conventional bulk parameterization scheme (see Fairall et al. (1996)
 208 for detailed description).

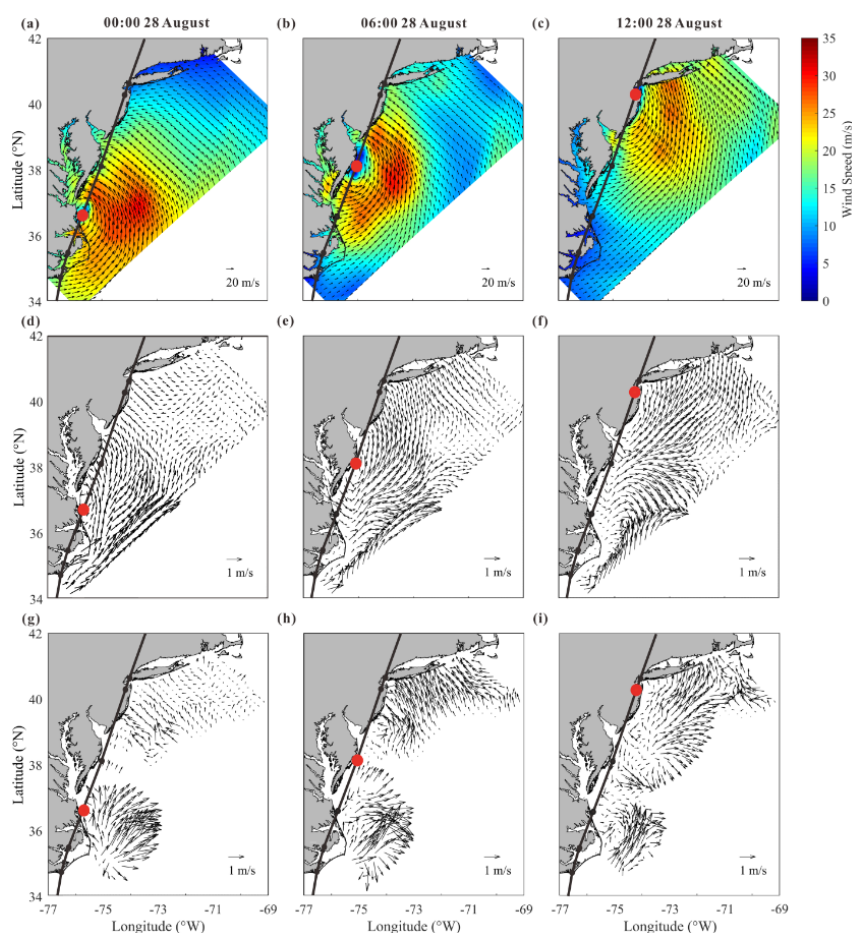
209 **3 Ocean Responses to Hurricane Irene**

210 **3.1 Effect of hurricane on ocean surface flow**

211 As shown in Figure 1, Hurricane Irene (2011) entered the Mid-Atlantic Bight (MAB)
 212 area of the present interest at Cape Lookout, North Carolina as a Category-1 event at 12:00,
 213 27 August, 2011 (UTC time, the same below) with a maximum sustained wind (MSW) of



214 over 38 m/s. It continued to move northeastward and made a landfall at Atlantic City, New
215 Jersey at 9:35, 28 August with a MSW of around 30 m/s. During its motion in the MAB area
216 of our interest, the radius of the hurricane wind field (the area with wind speed ≥ 32.9 m/s)
217 reached a large value of 140 km (Avila and Cangialosi, 2011).
218



219

220 Figure 2. Snapshots of (a-c) the 10-m wind provided by H*WIND, (d-f) computed current
221 velocity of the surface layer and (g-i) observed current velocity of the surface layer, at (left
222 column) 00:00, (middle column) 06:00 and (right column) 12:00, 28 August, during the
223 passage of Hurricane Irene (2011). Note that best track of the hurricane reported by Avila
224 and Cangialosi (2011) is shown by black lines while the hurricane center is shown by red
225 circles.

226



227 Figure 2 provides the snapshots of the wind, the computed and observed currents in
228 the MAB area at 00:00, 06:00 and 12:00, 28 August, 2011, respectively. Note that 00:00 and
229 12:00 correspond to the time when Hurricane Irene entered and left the area of our interest,
230 respectively. The wind field is plotted from the H*WIND data. Field currents are obtained
231 by analyzing data from a network of High Frequency Radar (HF Radar) stations (Roarty et
232 al., 2010) in the Mid-Atlantic Regional Association's Coastal Ocean Observing System
233 (MARACOOS, <https://maracoos.org/>). The field data have a temporal resolution of 1 hr and
234 a spatial resolution of 6 km, and are assumed to be measured at an effective depth of 2.4 m
235 below the ocean surface. The data cover the MAB area from the coast to the shelf break and
236 demonstrate a reasonably good accuracy when compared to data obtained with ADCP
237 (Acoustic Doppler Current Profiler), which are usually considered to be reliable (Liu et al,
238 2014).

239 The computed current velocity of the surface layer, as shown in Figure 2d-f, is
240 compared with the observed one, as shown in Figure 2g-i, to verify the reliability of the
241 numerical model presented in this study. At 00:00, 28 August, it is numerically demonstrated
242 that currents rotating counterclockwise with a magnitude of over 1 m/s are rapidly generated
243 by the wind near the hurricane center (Figure 2d). In the observed results, though there are
244 significant data missing near the hurricane center, northeastward currents can still be
245 identified on the offshore waters along North Carolina coast (Figure 2g) and are in
246 reasonable agreement with the computed current field. Moreover, both computational and
247 observational results support a fact that the onshore wind (Figure 2a) on the front side of the
248 hurricane drives an onshore current with magnitude of 0.4 m/s along the northern MAB,
249 especially in the nearshore area of New Jersey (Figure 2d and 2g). At 06:00, Hurricane Irene
250 arrived at the offshore waters of Delmarva Peninsula. In spite of the field data missing, the
251 rotating currents induced by the hurricane wind can be clearly recognized in both computed
252 and observed results in the nearshore area of New Jersey (Figure 2e and 2h). In addition,
253 relatively strong onshore currents with magnitude of over 1 m/s are observed near Long
254 Island and are also well represented in the numerical results (Figure 2e). At 12:00, i.e., the



255 time when the hurricane left the area of our interest, the counterclockwise rotating currents
256 are still formed near the hurricane center as demonstrated by both computational and
257 observational results (Figure 2f and 2i). At the same time, clockwise rotating currents are
258 shown to be generated near Delmarva Peninsula in southern MAB after the hurricane passed
259 over. This fact is certainly confirmed by both computed and observed results, indicating
260 near inertial currents are activated after the hurricane event. Therefore, it becomes evident
261 that the rotating wind of the hurricane immediately forces a rotating current in the surface
262 layer of the ocean and induces an inertial current rotating in the opposite direction shortly
263 after the hurricane passed over. It is also worthwhile to emphasize that, in general, the
264 numerical results obtained with the present model agree fairly well with observed data.

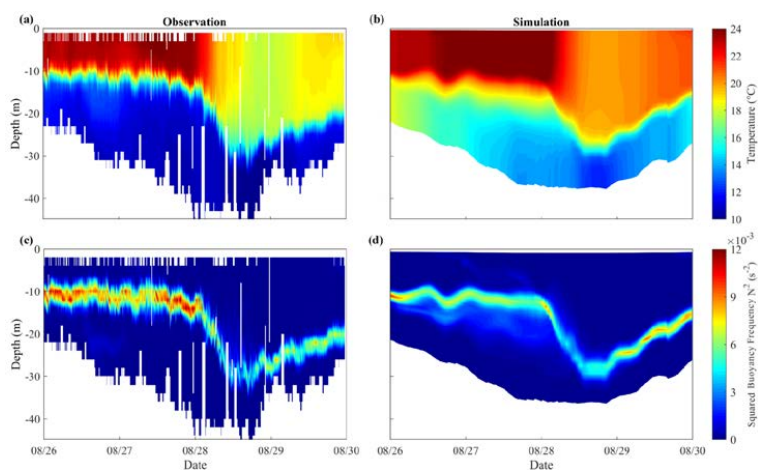
265 3.2 Effect of hurricane on vertical stratification and sea surface cooling

266 Shown in Figure 3a is the vertical profile of the seawater temperature measured by
267 Glider RU16 launched off the New Jersey Coast. Glider RU16 was an autonomous
268 underwater vehicle of the Slocum glider platform developed by Teledyne-Webb Research
269 (Schofield et al., 2007, 2010), which has demonstrated to be advantageous in marine
270 monitoring, particularly under extreme weather conditions (Glenn et al., 2016; Miles et al.,
271 2017; Seroka et al., 2016; Zhang et al., 2018). Glider RU16 can measure not only the vertical
272 profiles of seawater temperature and salinity but also the water depth. During the hurricane
273 event, its position may include a certain amount of drift in the horizontal directions due to
274 the ambient flow.

275 In Figure 3a, it is seen that the mixed layer off New Jersey coast was quite thin, with a
276 thickness of less than 10 m, before the hurricane event. A strong stratification was clearly
277 formed over a water depth of 40 m, with a surface temperature of 24 °C and a bottom
278 temperature of 10 °C. When the hurricane center passed over the position of Glider RU16
279 at around 09:30, 28 August, the thickness of the mixed layer rapidly increased to nearly 30
280 m while the surface temperature was decreased by more than 5 °C, indicating a strong
281 mixing process has occurred. By plotting the time series of the squared buoyancy frequency



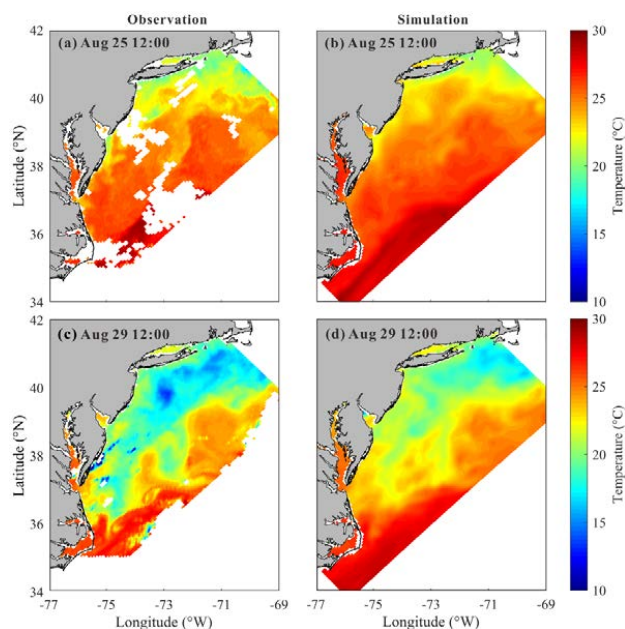
282 N based on the measured data, expansion of the mixed layer due to the hurricane event
 283 may be more vividly demonstrated (Figure 3c).
 284



285

286 Figure 3. Time series of the vertical profiles of (top row) the temperature and (bottom row)
 287 the squared buoyancy frequency, obtained from (a, c) Glider RU16 and (b, d) numerical
 288 model.
 289

290 Figure 3b and 3d present the computed results for the vertical distribution of seawater
 291 temperature obtained by virtually setting a measuring point moving with the glider in the
 292 real situation. The numerical results show a similar variation of the stratification pattern
 293 before and during the hurricane event, indicating that the numerical model is capable of
 294 describing the development and destruction of ocean stratification. However, a sea surface
 295 cooling of about 4 °C obtained by the numerical model is a little smaller than 6-7 °C
 296 observed by the glider in the field, probably due to the inaccurate setting of the initial bottom
 297 temperature in the computation. In fact, the initial condition for the bottom temperature in
 298 HYCOM is somehow higher (about 4°C) than the observed value in the field if Figures 3a
 299 and 3b are compared. To correct this system error, the real-time profile obtained from RU16
 300 is used for a nudging process in computation, i.e., the model temperature and salinity fields
 301 are forced to nudge toward observed data (see Thyng et al. (2021) for detailed description).
 302



303

304 Figure 4. Sea surface temperature at Aug 25 12:00, before the hurricane event (top row) and
 305 at Aug 29 12:00, after the hurricane event (bottom row) from (a, c) observed data and (b, d)
 306 numerical model.

307

308 The sea surface temperatures (SST) before and after the hurricane event are further
 309 compared in Figure 4 (obtained from The Advanced Very High Resolution
 310 Radiometer (AVHRR), <https://earth.esa.int/eogateway/catalog/avhrr-level-1b-local-area-coverage-imagery>). Before the hurricane event, both observed and computed SST show
 311 similar patterns, i.e., the SST decreases with the increasing latitude. After the hurricane
 312 passage, the strong cooling mainly takes place in shallow waters, where the mixing is strong
 313 (Zhang et al., 2016), especially near New Jersey and Long Island. However, cooling is not
 314 prominent in shallow waters near North Carolina. In fact, the SST in this region had
 315 decreased and then recovered to its pre-hurricane level previously (Seroka et al., 2016). It
 316 should be pointed out that the computed SST cooling is 3-4 °C smaller than the observed
 317 one, which could also be explained by the inaccurate initial condition obtained from
 318 HYCOM. The HYCOM bottom temperature is somehow higher than actual, which could
 319 lead to the underestimation of the SST cooling. Therefore, we use the real-time SST data
 320

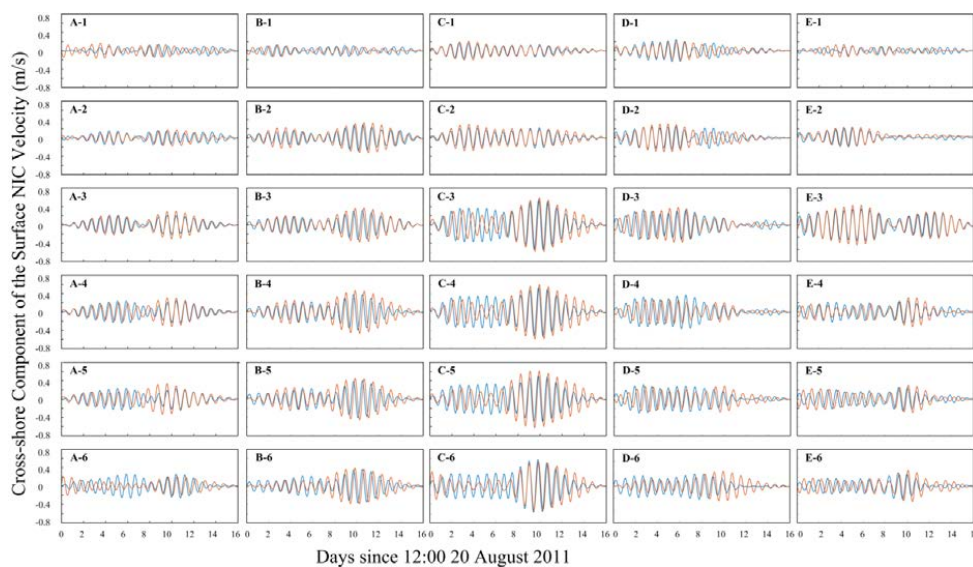


321 obtained from AVHRR for nudging process in computation to correct this system error
322 (Thyng et al., 2021). Note that the error is mainly caused by the discrepancy in initial
323 settings but not the defects in numerical method. Thus this error could be calibrated in
324 certain extent and thus would not affect the reliability of subsequent analysis, e.g. energy
325 budget analysis.

326 3.3 Characteristics of NIC

327 To have a general understanding of the NICs in the MAB area induced by Hurricane
328 Irene (2011), a network of 30 stations aligned on 5 cross-shore sections from south to north
329 is introduced in this study to cover the area of our interest as shown in Figure 1a, similar to
330 Zhang et al (2018). In each section, 6 stations are placed in the cross-shore direction from
331 the shore side to the deep ocean, where water depths are around 30 m, 50 m, 75 m, 120 m,
332 and 220 m and 1000 m, respectively. Note that the most offshore stations are located outside
333 the shelf break.

334 The velocity of NIC is obtained from the total current velocity by first excluding the
335 tidal components and then passing it through a Butterworth filter with the frequency band
336 of $0.8-1.2f_0$, an effective approach proposed by Hormann et al. (2014), Zhang et al. (2018)
337 and Kawaguchi et al. (2020). Shown in Figure 5 are the time series of surface velocity of
338 the NIC component in the cross-shore direction at all stations during the time period of our
339 study (16 days from 20 August to 5 September). The alongshore component was similar to
340 cross-shore component and thus omitted here. It is demonstrated that the numerical results
341 are in reasonably good agreement with the HF Radar data and the Pearson product-moment
342 correlation coefficient reaches 0.7 (Derrick et al., 1994). The major sources of error in the
343 measured data are found at the most offshore stations, such as A6 and D6, where the
344 coverage of HF Radar is limited. In fact, Roarty et al. (2010) indicated that the observed
345 data outside the shelf break should be used with caution. Error in the numerical results of
346 the NICs may come from the minor errors in the wind forcing data because they are very
347 sensitively related, e.g., underestimation at C3-C6 before the hurricane event may come
348 from the errors in low-resolution NAM data used in pre-hurricane periods.



349

350 Figure 5. Time series of the NIC velocity in the surface layer obtained (blue line) by the HF
 351 Radar and (orange line) with numerical model at 30 stations along sections A-E.

352

353 In Figure 5, it can be readily recognized that, in the cross-shore direction from shallow
 354 to deep waters (i.e., Station No.1-No.5 in present study), the NIC velocity gradually
 355 increases by a factor of at least three, e.g., from 0.15 m/s to 0.6 m/s in section C, which is
 356 consistent with conclusions in previous studies (Kim and Kosro, 2013; Yang et al., 2015;
 357 Rayson et al., 2015; Zhang et al., 2018). This is because that NIC velocity in the nearshore
 358 region are restricted due to a combination of several reasons presented by Chen and Xie
 359 (1997), Rayson et al. (2015) and Chen et al. (2017). Different from other studies, however,
 360 the NIC velocity in the deep waters (i.e., Station No. 6 in the present study) is found to be
 361 not larger or even smaller than that nearby the shelf break. This is probably due to that fact
 362 that the track of Hurricane Irene (2011) was nearly attached to the shore during its motion
 363 in the area of our interest and the wind stress over the deep ocean was relatively small. From
 364 south to north, it is found that the NIC velocity in the middle regions, such as along section
 365 C, is larger than those in south and north. By checking the numerical results, it is found that
 366 the stratification was only slightly destroyed during the hurricane event near section C as



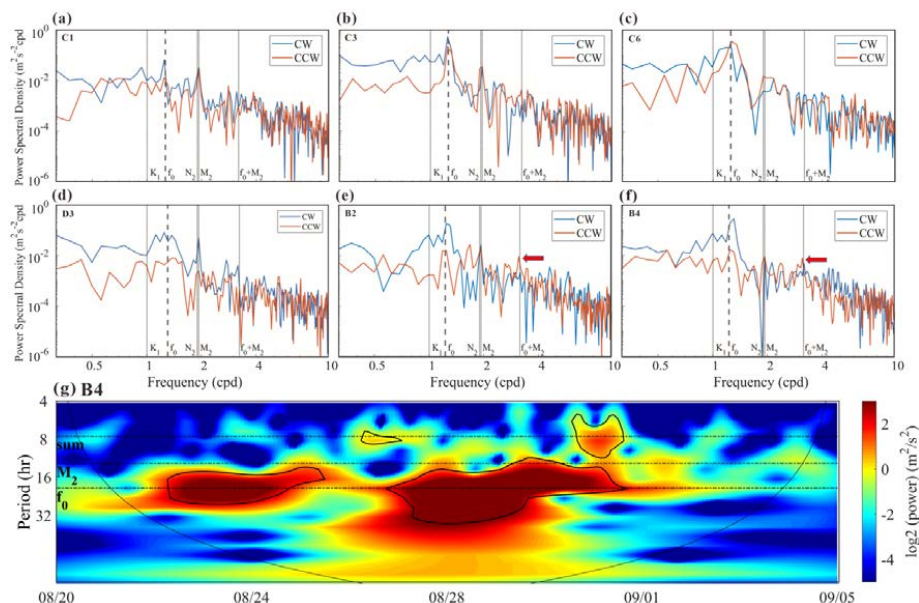
367 compared to the adjacent sections, which thus provided a better environment for NIC
368 generation (Yang et al., 2015; Shen et al., 2017).

369 To evaluate the relative importance of the near inertial currents, the rotary spectra of
370 the surface current velocity during the period of study (16 days) at different stations are
371 shown in Figure 6. The tidal flows corresponding to the major constituents M2, N2 and K1,
372 obtained with ADCIRC, are also plotted. It is seen that the velocity of the NICs is of an
373 equivalent magnitude to that of the M2 tidal current at the shallow-water stations where the
374 water depth is about 30 m (section C was taken for an example, Figure 6a). But, the velocity
375 of the NICs is significantly larger than that of the tidal current in deeper regions (Figure 6b,
376 c). It may be necessary to point out that weak NICs are not limited to the most nearshore
377 stations. In section D, for example, it is extended to a water depth of 75 m (Station D3,
378 Figure 6d). As discussed in the previous subsection, the weak NICs in the nearshore area
379 are closely related to the destruction of stratification by the strong mixing process associated
380 to the hurricane event (Yang et al., 2015; Shen et al., 2017). However, this effect does not
381 challenge the dominant role of NICs in deep waters.

382 Previous studies reported the nonlinear wave-wave interaction could transfer energy
383 from the M2 tide and NIC into a wave at the sum of their frequencies ($fM2$). The key
384 mechanism is the coupling between the vertical shear in NIC and the vertical velocity due
385 to the internal tide (Davis and Xing, 2003; Hopkins et al., 2014; Shen et al., 2017; Wu et al.,
386 2020). Though the M2 tide is rather strong in shallow waters during the hurricane event
387 (Figure 6), nonlinear wave-wave interaction between the tidal current and the NIC could be
388 hardly identified in most part of MAB. Nevertheless, a peak of the energy spectrum seems
389 to appear at the sum-frequency $fM2$ for the surface velocity at Stations B1 to B4, near
390 Delmarva Peninsula (B2 and B4 were taken as examples in Figure 6e, f). The evolution of
391 energy power at different frequencies for the middle-layer averaged (i.e., 10-30 m) currents,
392 where the flow shear is concentrated, is further demonstrated based on wavelet analysis
393 (Station B4 was taken as an example in Figure 6g). A peak energy at the sum-frequency $fM2$
394 is clearly identified after the hurricane passage. In fact, the subsequent Section 4.2 in this



395 paper will show that the strongest shear is found in offshore waters between Delmarva
 396 Peninsula and New Jersey, i.e., near sections B and C (Figure 8a). Besides, Brunner and
 397 Lwiza (2020) indicated that the most prominent M2 tide in southern MAB is located off
 398 Delmarva Peninsula (near section B), according to a long-term observed data. Therefore,
 399 the vertical shear in NIC and the vertical velocity due to the M2 tide is more likely to be
 400 coupled in this region (i.e., near section B). However, this interaction only occurs in limited
 401 regions and thus would not influence the NIC evolution in most part of MAB.
 402



403
 404 Figure 6. The rotary spectra of the current velocity in the surface layer during the simulation
 405 time (16 days) obtained by HF Radar at Stations (a) C1 (~30m), (b) C3 (~75m), (c) C6
 406 (~1000 m), (d) D3, (e) B2 and (f) B4. Clockwise and counter-clockwise components of the
 407 current are shown by blue and orange lines, respectively (NICs are considered to be
 408 dominated by the clockwise component). The frequencies of the major tidal constituents
 409 M2, N2 and K1, the inertial frequency f_0 , and the sum-frequency of M2 and f_0 are all marked
 410 by gray lines. (g) Wavelet power spectrum for 10-30 m depth-averaged alongshore current
 411 component at Station B4 (see Thiebaut and Vennell (2010) for detailed description). Black
 412 contours indicate the 5% significance level against red noise and the arc line indicate the
 413 cone of influence.



414 **4 Near Inertial Kinetic Energy**

415 **4.1 Conservation of NIKE**

416 For description of the intensity of a NIC, the near inertial kinetic energy (NIKE) may
417 be defined in the following way:

$$418 \quad E' = \frac{1}{2} \rho_0 |\mathbf{u}'|^2 \quad (12)$$

419 where, \mathbf{u}' is the velocity of the NIC; ρ_0 is the seawater density at the standard
420 atmospheric pressure. Note that the NIKE is mainly gained from the wind power and
421 dissipated due to a few mechanisms. Evolution of the vertically integrated NIKE within a
422 water column from the sea bottom to the ocean surface is thus governed by (Zhai et al., 2009)

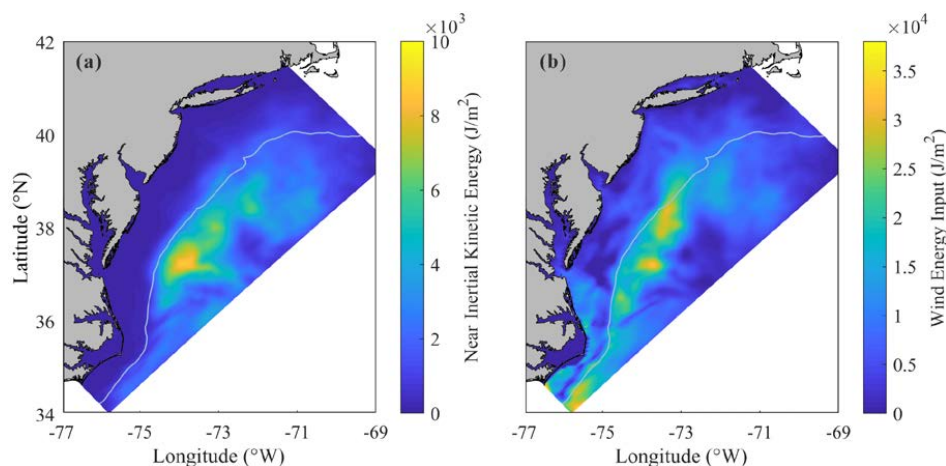
$$423 \quad \int_{-d}^{\eta} \frac{\partial E'}{\partial t} dz = \boldsymbol{\tau}_s \cdot \mathbf{u}'_s + \boldsymbol{\tau}_b \cdot \mathbf{u}'_b - \int_{-d}^{\eta} \rho_0 \nu_e \left| \frac{\partial \mathbf{u}'}{\partial z} \right|^2 dz - \quad (13)$$
$$\int_{-d}^{\eta} \nabla \cdot (\mathbf{u}' p') dz - \int_{-d}^{\eta} \rho' g w' dz - \int_{-d}^{\eta} \nabla \cdot (\mathbf{U} E') dz + \text{others}$$

424 where, \mathbf{u}'_s and \mathbf{u}'_b are near inertial velocities at sea surface and bottom, respectively; \mathbf{U}
425 is the sub-inertial velocity; ρ' is the perturbation density, defined by $\rho' = \rho - \rho_*$; ρ_* is
426 the reference density, i.e., the density corresponding to a flattened stratification where the
427 fluid is redistributed adiabatically to a stable and vertically uniform state from the actual
428 condition (Holliday and McIntyre, 1981; Kang and Fringer, 2010; MacCready and Giddings,
429 2016); p' is the perturbation pressure, defined by $p' = g \int_z^{\eta} \rho' dz$. Terms on the right-hand
430 side of Eq. (13) are the wind energy input, the dissipation due to bottom friction, the vertical
431 diffusion due to turbulence, the horizontal divergence of near inertial energy flux, the
432 conversion between kinetic and potential energy, and the advection of NIKE by the sub-
433 inertial flow. The last term 'others' includes nonlinear transfer of energy between NICs and
434 flows of other frequencies as well as the horizontal diffusion due to mixing. Note that the
435 energy are integrated over the water column from $z = -d$ to free surface $z = \eta$. In
436 shallow waters, d is the actual water depth, while in deep waters, d is truncated to 200
437 m (i.e., the depth of the shelf break). When the bottom boundary is set at $z = -200$ m,



438 the bottom friction vanishes in Eq. (13) but a term related to the downward energy flux, i.e.,
 439 $p'w'|_{z=-200m}$ should be added.

440 For a general understanding, distribution of the depth-integrated NIKE averaged over
 441 a 10-day period from August 25 to September 4 is presented in Figure 7a. The wind power
 442 integrated over the same period is plotted in Figure 7b. It is clearly shown in Figure 7a that
 443 the high NIKE region mainly located in the offshore waters of Delmarva Peninsula and New
 444 Jersey rather than in the nearshore area. This distribution pattern is rather similar to that of
 445 the wind energy input, as presented in Figure 7b, indicating that the NIKE was immediately
 446 gained from the wind power (Rayson et al. 2015; Shen et al., 2017; Zhang et al., 2018). In
 447 fact, the NIKE could also come from other processes apart from the wind energy input
 448 (Alford et al, 2016), meanwhile the wind energy input may also be transferred to energy of
 449 waves apart from NIC (Chen et al., 2017), which leads to differences between Figure 7a and
 450 7b.
 451



452
 453 Figure 7. Spatial distribution of (a) depth-integrated near inertial kinetic energy averaged
 454 over the 10-day period and (b) wind power input to NICs integrated over the 10-day period.
 455
 456



457 Table 1. The contribution of each mechanism to energy budget. Percentages in parentheses
458 refer to the ratio of each factor to wind energy input.

Factor (J)	Contribution in Region A	Contribution in Region B
Wind Energy Input	7.75×10^{14}	3.16×10^{14}
Vertical Turbulence Diffusion	3.12×10^{14} (40%)	2.12×10^{14} (67%)
Lateral Divergence	1.34×10^{14} (17%)	5.69×10^{13} (18%)
Downward Transfer	2.58×10^{14} (33%)	0
Advection	3.33×10^{13} (4%)	1.04×10^{13} (3%)
Conversion	6.9×10^{12} (1%)	1.58×10^{13} (5%)
Bottom Friction	0	7.58×10^{13} (24%)

459

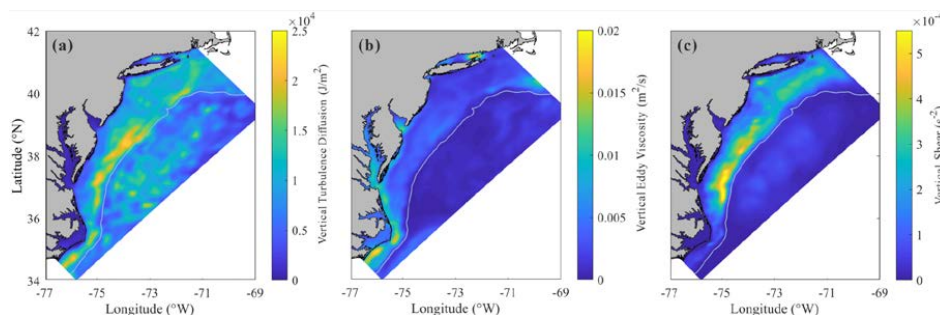
460 An important objective of the present study is to identify the mechanism of NIC
461 development and decay. For this purpose, we consider a rectangular domain and separate it
462 into deep water region A (depth > 200 m) and continental shelf region B (depth ≤ 200 m),
463 as depicted in Figure 1a. If the NICs are considered to be negligibly weak before and after
464 Hurricane Irene (2011), we may try to find how the wind power that drives the NICs during
465 the hurricane event is balanced, by comparing the accumulated contribution of different
466 mechanisms. Performing an integration of each terms in Eq. (13) with respect to time over
467 10 days from August 25 to September 4 and with respect to the horizontal coordinates over
468 both deep water region A and continental shelf region B, the contribution of each mechanism
469 to the energy budget is obtained as shown in Table 1. It is clearly demonstrated that in the
470 deep water region, the wind energy input was basically balanced by the vertical diffusion
471 due to turbulence (40%) and a downward transfer of the near inertial energy to the deep
472 ocean (33%). In the continental shelf region, the vertical diffusion due to turbulence
473 dominated the dissipation of NIKE (nearly 70%), while the bottom friction played a
474 secondary role (24%). It is worthwhile mentioning that lateral divergence of NIKE should
475 not be neglected in both shallow and deep water regions under the hurricane condition



476 (nearly 20%), different from previous studies which focused on NICs under the local wind
477 condition or in a broader research region across the whole North Atlantic (Chant, 2001; Zhai
478 et al., 2009; Shen et al., 2017). Other processes, e.g., advection due to sub-inertial flows,
479 only played a minor role. Note that the ratio of near inertial energy decay to wind energy
480 input exceeded 100% in the continental shelf region, confirming that NIKE may be gained
481 from other sources in addition to wind energy input in nearshore regions (Alford et al., 2016).

482 4.2 Decay of NIKE

483 The spatial distribution of the time-integrated energy dissipated through vertical
484 diffusion due to turbulence is plotted in Figure 8a. It is seen that a large amount of the
485 dissipation occurred at the offshore side of the continental shelf (i.e., at the offshore side of
486 the shallow region B), which does not coincide with the region where the wind energy input
487 is intense as demonstrated in Figure 7b. This implies that dissipation of NIKE is not mainly
488 caused by an increased intensity of turbulence, which certainly takes place in a region where
489 wind energy input achieves a high level (Zhai et al., 2009; Zhang et al., 2018). For a more
490 detailed discussion, the averaged eddy viscosity ν_e and the averaged vertical shear rate of
491 NIC $|\partial \mathbf{u}' / \partial z|^2$ during the period of our study are presented in Figure 8b and 8c. It is then
492 confirmed that the strong vertical shear also occurred at the outer half of the continental
493 shelf. The eddy viscosity, however, has a completely different distribution. In conclusion,
494 the vertical shear, known to be closely related to the ocean stratification (Shen et al., 2017),
495 plays a crucial role in the turbulence diffusion. It happened that one of the well-known
496 sharpest thermoclines in the world exists in the coastal water of MAB (Schofield et al., 2008;
497 Lentz, 2017). It may be necessary to emphasize that, although the stratification in the
498 shallowest water was totally destroyed during the hurricane event, as mentioned in Section
499 3, the seawater at the outer half of the continental shelf still partly maintained its
500 stratification.



501

502 Figure 8. Spatial distribution of (a) depth-integrated vertical diffusion due to turbulence
 503 integrated over the 10-day period, (b) depth-averaged vertical eddy viscosity and (c) depth-
 504 averaged vertical shear, both averaged over the 10-day period.

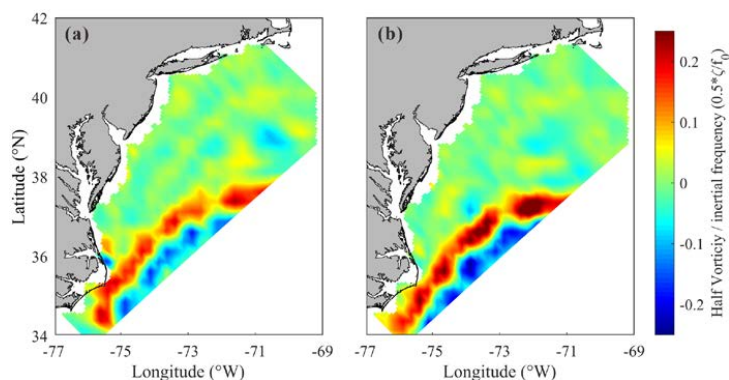
505

506 The lateral divergence of NIKE flux, which also results in decay of NIKE and is not
 507 trivial (~20%) in both shallow and deep water regions, may have to be discussed in some
 508 details. As shown in Eq. (13), the lateral divergence of NIKE flux is a vertical integration
 509 of $\nabla \cdot (\mathbf{u}'p')$, which may also be expressed as an equivalent integration of $\nabla \cdot (\mathbf{c}'E')$,
 510 where \mathbf{c}' is the transport velocity of NIKE in the horizontal plane (Price, 1994). When
 511 compared to previous studies (Zhai et al., 2009), which dealt with the normal wind induced
 512 NIC over a large part of the North Atlantic and showed that the lateral divergence accounted
 513 only for less than 5% of the total NIKE loss, we focused only on the hurricane-affected
 514 region. In the hurricane-affected region, the larger NIKE gradient naturally leads to a larger
 515 divergence. If we extend the domain of study by a factor of 1.5, however, contribution of
 516 the averaged lateral divergence decreases by more than half. It is thus strongly implied that
 517 the lateral divergence of NIKE flux is significant within the hurricane-affected region.

518 It is also of interest to note that the contribution of the lateral divergence in south region
 519 of our computational domain is less than 8%, much smaller than the average value of ~20%.
 520 Several studies have pointed out that the transport velocity \mathbf{c}' is largely influenced by the
 521 background vorticity gradient (Zhai et al., 2009; Park et al., 2009). In other words, NIKE
 522 can hardly be transferred from a place of lower background vorticity to a place of higher
 523 background vorticity or, NIKE can hardly penetrate a vorticity ridge from either side. Shown
 524 in Figure 9 is the distribution of the background vorticity within our computational domain



525 during the hurricane event (data from [https://resources.marine.copernicus.eu/product-](https://resources.marine.copernicus.eu/product-detail/SEALEVEL_GLO_PHY_CLIMATE_L4_MY_008_057/INFORMATION)
526 [detail/SEALEVEL_GLO_PHY_CLIMATE_L4_MY_008_057/INFORMATION](https://resources.marine.copernicus.eu/product-detail/SEALEVEL_GLO_PHY_CLIMATE_L4_MY_008_057/INFORMATION)). A
527 remarkable vorticity ridge exists in the southeast of the computational domain, which is
528 considered to be caused by the strong horizontal shear at the edge of Gulf Stream (a warm
529 and swift ocean current in Atlantic, flowing through the southern MAB and propagating
530 northeastward). This vorticity ridge can reduce the lateral divergence of NIKE flux in south
531 region of our computational domain.



532

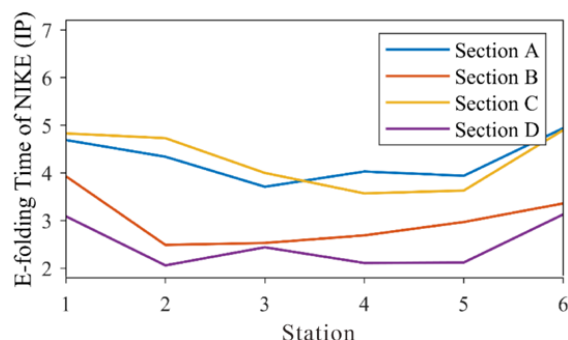
533 Figure 9. Spatial distribution of background vorticity (a) before the hurricane event on Aug
534 25 and (b) after the hurricane event on Sep 4.

535

536 4.3 Decay timescale of NIKE

537 It is of practical importance to determine the rate of NIKE decay. A conventional
538 measure of the rate of NIKE may be its e-folding time, i.e., the timescale in which the NIKE
539 decreases by a factor of e. Shown in Figure 10 is the e-folding time of the depth-integrated
540 NIKE at 24 stations along sections A to D. The decay timescale in section E is not considered
541 because this section is relatively far from the hurricane track as compared with other
542 sections and also because the orientation of section E differs quite significantly from that of
543 other sections.

544



545

546 Figure 10. The decay timescale of the depth-integrated NIKE at 24 stations along sections
547 A to D. Note that the unit for the e-folding time is the inertial period.

548

549 It is interesting to note that the decay timescales in the shallow and deep regions are
550 fairly different. As shown in Figure 10, the NIKE is dissipated much more slowly outside
551 the shelf break (Station No.6) than over the continental shelf. This difference is often
552 considered to be an effect of the bottom friction and the extremely strong turbulence in the
553 shallow waters, as pointed out by other researchers (Rayson et al., 2015; Shen et al., 2017).
554 It is also interesting to find that the variation of NIKE decay rate in shallow waters is much
555 more complicated than in the deep waters. In the cross-shore direction, the NIKE at the
556 middle stations, i.e., Stations No. 3 to No. 5, located at the outer half of the continental shelf,
557 is shown to be dissipated most rapidly, especially along sections A to C (Figure 10). This
558 phenomenon is actually supported by the fact that the strongest turbulence diffusion
559 occurred over the outer half of the continental shelf, particularly in the relevant region
560 between sections A and C (Figure 8a). Considering the variation of the wind energy input
561 within the same section should not be too large, the ratio of turbulence diffusion to wind
562 energy input must be mainly determined by the turbulence diffusion. Therefore, the strong
563 turbulence dissipation due to the strong vertical shear in well-maintained stratification is
564 responsible for the rapid energy decay in the outer half of the continental shelf, as shown in
565 Section 4.2. Although the bottom friction also has some effect on the decay timescale of
566 NIKE onshore, the turbulence effect is predominant.



567 In the alongshore direction, it is shown that the NIKE in sections B and D decayed
568 more rapidly. Actually, the decay timescale there is only 2 to 3 inertial periods compared to
569 4 to 5 inertial periods in sections A and C. However, the limited variability of the turbulence
570 diffusion in alongshore direction should not lead to such a big difference. Near section A,
571 the vorticity ridge in Gulf Stream restricted the lateral divergence of NIKE, which may
572 contribute to a long decay timescale to some extent. However, the role of this effect was
573 limited. In fact, as mentioned in Section 3, the nonlinear wave-wave interaction near section
574 B may have caused a transfer of NIKE to other frequencies, as also pointed out by Shen et
575 al. (2017). In fact, it is found that the ratio of turbulence diffusion to wind input in section
576 B was larger than in other sections by 20%-30%, due to the low level of wind input (Figure
577 7b) and high level of turbulence dissipation (Figure 8a) there. These factors combined seem
578 to have yielded an extraordinarily short e-folding time in section B. In section D, due to the
579 complete destruction of stratification after the hurricane event (as mentioned in Section 3
580 and shown in Figure 6d), the NICs were of the same order as the background flow (D1-D4
581 in Figure 5). Therefore, the decay timescale of NIKE in section D is certainly inaccurate
582 and possibly meaningless.

583 **5 Conclusion**

584 This study is aimed to investigate the development and decay mechanism of NICs in
585 the MAB area caused by Hurricane Irene (2011). Numerical results obtained with ROMS
586 are shown to agree well with the observational data. Both computational and observational
587 results show that the rotating wind of the hurricane immediately forced a rotating current in
588 the surface layer of the ocean and induced an inertial current rotating in the opposite
589 direction about one inertial period after the hurricane passed over. The NICs overwhelmed
590 M2 tide in most areas of the MAB region except in the nearshore area where the
591 stratification was totally destroyed by the strong mixing due to turbulence. In addition, the
592 cross-shore component of the NIC velocity gradually increases by a factor of at least three
593 from a shallow-water position to the shelf break.



594 The energy budget in the NICs is investigated in both deep and shallow waters. NIKE
595 was shown to be immediately gained from the wind power during the hurricane event. In
596 the deep water region, NIKE was mainly dissipated by the vertical diffusion due to
597 turbulence and partially transferred to deep waters. In the continental shelf region, NIKE
598 was basically dissipated by the turbulence diffusion, meanwhile the bottom friction played
599 a secondary role. The nonlinear wave-wave interaction only dissipated NIKE in limited
600 regions, e.g. shelf waters off Delmarva Peninsula. Notably, the lateral divergence of NIKE
601 should be taken into consideration in both shallow and deep water regions under the
602 hurricane condition. However, in southern MAB, it was restricted by a vorticity ridge at the
603 edge of Gulf Stream. It is also clarified that the NIKE dissipation due to turbulence diffusion
604 is much more closely related to the rate of the vertical shear rather than the intensity of
605 turbulence, which certainly takes place in a region where wind energy input achieves a high
606 level. The strong vertical shear at the offshore side of the continental shelf led to the
607 strong turbulence dissipation in this region.

608 **Competing interests**

609 The authors declare that there is no conflict of interest.

610 **Authors' contributions**

611 P. Han and X. Yu conceived of the presented idea. P. Han performed the computations.
612 X. Yu supervised the project. Both authors discussed the results and contributed to the final
613 manuscript.

614 **Funding**

615 This research is supported by National Natural Science Foundation of China (NSFC)
616 under grant No. 11732008.



617 **Data Availability**

618 The data used in this study are listed below. In particular, the regional oceanic modeling
619 system (ROMS) code is available at <https://www.myroms.org>; HF radar data is available at
620 [http://tds.marine.rutgers.edu/thredds/dodsC/cool/codar/totals/5Mhz_6km_realtime_fmrc/
621 Maracoos_5MHz_6km_Totals-FMRC_best.ncd.html](http://tds.marine.rutgers.edu/thredds/dodsC/cool/codar/totals/5Mhz_6km_realtime_fmrc/Maracoos_5MHz_6km_Totals-FMRC_best.ncd.html); Glider data is available at
622 [http://tds.marine.rutgers.edu/thredds/dodsC/cool/glider/mab/Gridded/20110810T1330_epa
623 _ru16_active.nc.html](http://tds.marine.rutgers.edu/thredds/dodsC/cool/glider/mab/Gridded/20110810T1330_epa_ru16_active.nc.html); HYCOM data is available at [https://www.hycom.org/data/glb00pt08/
624 expt-91pt2](https://www.hycom.org/data/glb00pt08/expt-91pt2); ADCIRC data is available at <https://adcirc.org/products/adcirc-tidal-databases>;
625 USGS data is available at <https://waterdata.usgs.gov>; H*WIND data is available at
626 https://www.aoml.noaa.gov/hrd/data_sub/wind.html; NAM data is available at
627 [https://www.ncdc.noaa.gov/data-access/model-data/model-datasets/north-american-
628 mesoscale-forecast-system-nam](https://www.ncdc.noaa.gov/data-access/model-data/model-datasets/north-american-mesoscale-forecast-system-nam); C3S data is available at
629 [https://resources.marine.copernicus.eu/product-detail/SEALEVEL_GLO_PHY
630 _CLIMATE_L4_MY_008_057/INFORMATION](https://resources.marine.copernicus.eu/product-detail/SEALEVEL_GLO_PHY_CLIMATE_L4_MY_008_057/INFORMATION); AVHRR data is available at
631 <https://earth.esa.int/eogateway/catalog/avhrr-level-1b-local-area-coverage-imagery>.

632 **References**

633 Alford, M.H., 2003a. Improved global maps and 54-year history of wind-work on ocean
634 inertial motions. *Geophysical Research Letters*, 30(8).
635 Alford, M.H., 2003b. Redistribution of energy available for ocean mixing by long-range
636 propagation of internal waves. *Nature*, 423(6936): 159-162.
637 Alford, M.H., MacKinnon, J.A., Simmons, H.L. and Nash, J.D., 2016. Near-inertial internal
638 gravity waves in the ocean. *Annual Review of Marine Science*, 8(1): 95-123.
639 Allahdadi, M., 2014. Numerical experiments of hurricane impact on vertical mixing and de-
640 stratification of the louisiana shelf waters. Ph. D. Thesis, Louisiana State University,
641 Baton Rouge.
642 Amante, C. and Eakins, B.W., 2009. Etopo1 1 arc-minute global relief model: Procedures,
643 data sources and analysis. NOAA Technical Memorandum NESDIS NGDC-24,



- 644 National Geophysical Data Center, NOAA.
- 645 Avila, L.A. and Cangialosa, J., 2011. Tropical cyclone report: Hurricane irene: August 21–
646 28, 2011. National Hurricane Center Report AL0920011, US National Oceaninc and
647 Atmospheric Administration's National Weather Service.
- 648 Brunner, K. and Lwiza, K.M.M., 2020. Tidal velocities on the mid-atlantic bight continental
649 shelf using high-frequency radar. *Journal of Oceanography*, 76(4): 289-306.
- 650 Castelao, R.M., 2014. Mesoscale eddies in the south atlantic bight and the gulf stream
651 recirculation region: Vertical structure. *Journal of Geophysical Research: Oceans*,
652 119(3): 2048-2065.
- 653 Chang, S.W. and Anthes, R.A., 1978. Numerical simulations of the ocean's nonlinear,
654 baroclinic response to translating hurricanes. *Journal of Physical Oceanography*,
655 8(3): 468-480.
- 656 Chant, R.J., 2001. Evolution of near-inertial waves during an upwelling event on the new
657 jersey inner shelf. *Journal of Physical Oceanography*, 31(3): 746-764.
- 658 Chassignet, E.P. et al., 2007. The hycom (hybrid coordinate ocean model) data assimilative
659 system. *Journal of Marine Systems*, 65(1): 60-83.
- 660 Chen, C., Reid, R.O. and Nowlin Jr, W.D., 1996. Near-inertial oscillations over the texas-
661 louisiana shelf. *Journal of Geophysical Research: Oceans*, 101(C2): 3509-3524.
- 662 Chen, C. and Xie, L., 1997. A numerical study of wind-induced, near-inertial oscillations
663 over the texas-louisiana shelf. *Journal of Geophysical Research: Oceans*, 102(C7):
664 15583-15593.
- 665 Chen, G., Xue, H., Wang, D. and Xie, Q., 2013. Observed near-inertial kinetic energy in the
666 northwestern south china sea. *Journal of Geophysical Research: Oceans*, 118(10):
667 4965-4977.
- 668 Chen, S., Chen, D. and Xing, J., 2017. A study on some basic features of inertial oscillations
669 and near-inertial internal waves. *Ocean Science*, 13(5): 829-836.
- 670 Chen, Y. and Yu, X., 2016. Enhancement of wind stress evaluation method under storm
671 conditions. *Climate Dynamics*, 47(12): 3833-3843.



- 672 Chen, Y., Zhang, F., Green, B.W. and Yu, X., 2018. Impacts of ocean cooling and reduced
673 wind drag on hurricane katrina (2005) based on numerical simulations. *Monthly*
674 *Weather Review*, 146(1).
- 675 Churchill, J.H., Wirick, C.D., Flagg, C.N. and Pietrafesa, L.J., 1994. Sediment resuspension
676 over the continental shelf east of the delmarva peninsula. *Deep Sea Research Part II:*
677 *Topical Studies in Oceanography*, 41(2): 341-363.
- 678 Cummings, J.A., 2005. Operational multivariate ocean data assimilation. *Quarterly Journal*
679 *of the Royal Meteorological Society*, 131(613): 3583-3604.
- 680 D'Asaro, E.A., 1985. The energy flux from the wind to near-inertial motions in the surface
681 mixed layer. *Journal of Physical Oceanography*, 15: 1043-1059.
- 682 Davies, A.M. and Xing, J., 2003. On the interaction between internal tides and wind-induced
683 near-inertial currents at the shelf edge. *Journal of Geophysical Research: Oceans*,
684 108(C3).
- 685 Derrick, T.R., Bates, B.T. and Dufek, J.S., 1994. Evaluation of time-series data sets using
686 the pearson product-moment correlation coefficient. *Medicine and science in sports*
687 *and exercise*, 26(7): 919-928.
- 688 Donelan, M.A. et al., 2004. On the limiting aerodynamic roughness of the ocean in very
689 strong winds. *Geophysical Research Letters*, 31(18).
- 690 Dorostkar, A., Boegman, L., Diamessis, P. and Pollard, A., 2010. Sensitivity of mitgcm to
691 different model parameters in application to cayuga lake. *Proceedings of the 6th*
692 *International Symposium on Environmental Hydraulics, Two Volume Set*, p.^pp.
693 373-378.
- 694 Emanuel, K.A., 1995. Sensitivity of tropical cyclones to surface exchange coefficients and
695 a revised steady-state model incorporating eye dynamics. *Journal of the*
696 *Atmospheric Sciences*, 52: 3969-3976.
- 697 Fairall, C.W., Bradley, E.F., Rogers, D.P., Edson, J.B. and Young, G.S., 1996. Bulk
698 parameterization of air-sea fluxes for tropical ocean-global atmosphere coupled-
699 ocean atmosphere response experiment. *Journal of Geophysical Research: Oceans*,



- 700 101(C2): 3747-3764.
- 701 Freeman, N.G., Hale, A.M. and Danard, M.B., 1972. A modified sigma equations' approach
702 to the numerical modeling of great lakes hydrodynamics. *Journal of Geophysical*
703 *Research* 77(6): 1050-1060.
- 704 Furuichi, N., Hibiya, T. and Niwa, Y., 2008. Model-predicted distribution of wind-induced
705 internal wave energy in the world's oceans. *Journal of Geophysical Research:*
706 *Oceans*, 113(C9).
- 707 Garrett, C., 2001. What is the “near-inertial” band and why is it different from the rest of
708 the internal wave spectrum? *Journal of Physical Oceanography*, 31(4): 962-971.
- 709 Glenn, S.M. et al., 2016. Stratified coastal ocean interactions with tropical cyclones. *Nature*
710 *Communications*, 7(1): 10887.
- 711 Gregg, M.C., 1987. Diapycnal mixing in the thermocline: A review. *Journal of Geophysical*
712 *Research: Oceans*, 92(C5): 5249-5286.
- 713 Haidvogel, D.B. et al., 2008. Ocean forecasting in terrain-following coordinates:
714 Formulation and skill assessment of the regional ocean modeling system. *Journal of*
715 *Computational Physics*, 227(7): 3595-3624.
- 716 Hoarfrost, A. et al., 2019. Gulf stream ring water intrusion on the mid-atlantic bight
717 continental shelf break affects microbially driven carbon cycling. 6.
- 718 Holliday, D. and McIntyre, M.E., 1981. On potential energy density in an incompressible,
719 stratified fluid. *Journal of Fluid Mechanics*, 107: 221-225.
- 720 Hopkins, J.E., Stephenson Jr, G.R., Green, J.A.M., Inall, M.E. and Palmer, M.R., 2014.
721 Storms modify baroclinic energy fluxes in a seasonally stratified shelf sea: Inertial-
722 tidal interaction. *Journal of Geophysical Research: Oceans*, 119(10): 6863-6883.
- 723 Hormann, V., Centurioni, L.R., Rainville, L., Lee, C.M. and Braasch, L.J., 2014. Response
724 of upper ocean currents to typhoon fanapi. *Geophysical Research Letters*, 41(11):
725 3995-4003.
- 726 Jackett, D.R. and McDougall, T.J., 1995. Minimal adjustment of hydrographic profiles to
727 achieve static stability. *Journal of Atmospheric and Oceanic Technology*, 12(2): 381-



- 728 389.
- 729 Janjic, Z.I. et al., 2004, June. The ncep wrf core, 20th Conference on Weather Analysis and
730 Forecasting/16th Conference on Numerical Weather Prediction, Seattle, Washington,
731 pp. 10-25.
- 732 Jochum, M. et al., 2013. The impact of oceanic near-inertial waves on climate. *Journal of*
733 *Climate*, 26(9): 2833-2844.
- 734 Kang, D. and Fringer, O., 2010. On the calculation of available potential energy in internal
735 wave fields. *Journal of Physical Oceanography*, 40(11): 2539-2545.
- 736 Kawaguchi, Y., Wagawa, T. and Igeta, Y., 2020. Near-inertial internal waves and multiple-
737 inertial oscillations trapped by negative vorticity anomaly in the central sea of japan.
738 *Progress in Oceanography*, 181: 102240.
- 739 Kim, S.Y. and Kosro, P.M., 2013. Observations of near-inertial surface currents off oregon:
740 Decorrelation time and length scales. *Journal of Geophysical Research: Oceans*,
741 118(7): 3723-3736.
- 742 Kunze, E., 1985. Near-inertial wave propagation in geostrophic shear. *Journal of Physical*
743 *Oceanography*, 15(5): 544-565.
- 744 Lentz, S.J., 2017. Seasonal warming of the middle atlantic bight cold pool. *Journal of*
745 *Geophysical Research: Oceans*, 122(2): 941-954.
- 746 Li, M., Zhong, L., Boicourt, W.C., Zhang, S. and Zhang, D.-L., 2007. Hurricane-induced
747 destratification and restratification in a partially-mixed estuary. *Journal of Marine*
748 *Research*, 65(2): 169-192.
- 749 Liu, Y., Weisberg, R.H. and Merz, C.R., 2014. Assessment of codar seasonde and wera hf
750 radars in mapping surface currents on the west florida shelf. *Journal of Atmospheric*
751 *and Oceanic Technology*, 31(6): 1363-1382.
- 752 MacCready, P. and Giddings, S.N., 2016. The mechanical energy budget of a regional ocean
753 model. *Journal of Physical Oceanography*, 46(9): 2719-2733.
- 754 MacKinnon, J.A. and Gregg, M.C., 2005. Near-inertial waves on the new england shelf:
755 The role of evolving stratification, turbulent dissipation, and bottom drag. *Journal*



- 756 of Physical Oceanography, 35(12): 2408-2424.
- 757 Marchesiello, P., McWilliams, J.C. and Shchepetkin, A., 2001. Open boundary conditions
758 for long-term integration of regional oceanic models. *Ocean Modelling*, 3(1): 1-20.
- 759 Miles, T., Seroka, G. and Glenn, S., 2017. Coastal ocean circulation during hurricane sandy.
760 *Journal of Geophysical Research: Oceans*, 122(9): 7095-7114.
- 761 Mulligan, R.P. and Hanson, J.L., 2016. Alongshore momentum transfer to the nearshore
762 zone from energetic ocean waves generated by passing hurricanes. *Journal of*
763 *Geophysical Research: Oceans*, 121(6): 4178-4193.
- 764 Munk, W. and Wunsch, C., 1998. Abyssal recipes ii: Energetics of tidal and wind mixing.
765 *Deep Sea Research Part I: Oceanographic Research Papers*, 45(12): 1977-2010.
- 766 Olabarrieta, M., Warner, J.C. and Kumar, N., 2011. Wave-current interaction in willapa bay.
767 *Journal of Geophysical Research: Oceans*, 116(C12).
- 768 Park, J.J., Kim, K. and Schmitt, R.W., 2009. Global distribution of the decay timescale of
769 mixed layer inertial motions observed by satellite-tracked drifters. *Journal of*
770 *Geophysical Research: Oceans*, 114(C11).
- 771 Pollard, R.T., 1980. Properties of near-surface inertial oscillations. *Journal of Physical*
772 *Oceanography*, 10(3): 385-398.
- 773 Powell, M.D., Houston, S.H., Amat, L.R. and Morisseau-Leroy, N., 1998. The hrd real-time
774 hurricane wind analysis system. *Journal of Wind Engineering and Industrial*
775 *Aerodynamics*, 77-78: 53-64.
- 776 Powell, M.D., Vickery, P.J. and Reinhold, T.A., 2003. Reduced drag coefficient for high
777 wind speeds in tropical cyclones. *Nature*, 422(6929): 279-283.
- 778 Price, J.F., 1983. Internal wave wake of a moving storm. Part i. Scales, energy budget and
779 observations. *Journal of Physical Oceanography*, 13(6): 949-965.
- 780 Price, J.F., Sanford, T.B. and Forristall, G.Z., 1994. Forced stage response to a moving
781 hurricane. *Journal of Physical Oceanography*, 24(2): 233-260.
- 782 Rayson, M.D. et al., 2015. Near-inertial ocean response to tropical cyclone forcing on the
783 australian north-west shelf. *Journal of Geophysical Research: Oceans*, 120(12):



- 784 7722-7751.
- 785 Rimac, A., von Storch, J.-S., Eden, C. and Haak, H., 2013. The influence of high-resolution
786 wind stress field on the power input to near-inertial motions in the ocean.
787 Geophysical Research Letters, 40(18): 4882-4886.
- 788 Roarty, H. et al., 2010. Operation and application of a regional high-frequency radar
789 network in the mid-atlantic bight. Marine Technology Society Journal, 44(6): 133-
790 145.
- 791 Rodi, W., 1987. Examples of calculation methods for flow and mixing in stratified fluids.
792 Journal of Geophysical Research: Oceans, 92(C5): 5305-5328.
- 793 Sanford, T.B., Price, J.F. and Garton, J.B., 2011. Upper-ocean response to hurricane frances
794 (2004) observed by profiling em-apex floats. Journal of Physical Oceanography,
795 41(6): 1041-1056.
- 796 Schofield, O. et al., 2008. The decadal view of the mid-atlantic bight from the coolroom: Is
797 our coastal system changing? Oceanography, 21(4): 108-117.
- 798 Schofield, O. et al., 2007. Slocum gliders: Robust and ready. Journal of Field Robotics,
799 24(6): 473-485.
- 800 Schofield, O. et al., 2010. A regional slocum glider network in the mid-atlantic bight
801 leverages broad community engagement. Marine Technology Society Journal, 44(6):
802 185-195.
- 803 Seroka, G. et al., 2016. Hurricane irene sensitivity to stratified coastal ocean cooling.
804 Monthly Weather Review, 144(9): 3507-3530.
- 805 Shchepetkin, A.F. and McWilliams, J.C., 2005. The regional oceanic modeling system
806 (roms): A split-explicit, free-surface, topography-following-coordinate oceanic
807 model. Ocean Modelling, 9(4): 347-404.
- 808 Shearman, R.K., 2005. Observations of near-inertial current variability on the new england
809 shelf. Journal of Geophysical Research: Oceans, 110(C2).
- 810 Shen, J., Qiu, Y., Zhang, S. and Kuang, F., 2017. Observation of tropical cyclone-induced
811 shallow water currents in taiwan strait. Journal of Geophysical Research: Oceans,



- 812 122(6): 5005-5021.
- 813 Steiner, A. et al., 2017. Critical weather situations for renewable energies-part a: Cyclone
814 detection for wind power. *Renewable Energy*, 101: 41-50.
- 815 Stommel, H., 2020. *The Gulf Stream*. University of California Press.
- 816 Thiebaut, S. and Vennell, R., 2010. Observation of a fast continental shelf wave generated
817 by a storm impacting newfoundland using wavelet and cross-wavelet analyses.
818 *Journal of Physical Oceanography*, 40(2): 417-428.
- 819 Thyng, K.M. et al., 2021. Performance of offline passive tracer advection in the regional
820 ocean modeling system (roms; v3.6, revision 904). *Geoscientific Model
821 Development*, 14(1): 391-407.
- 822 Toffoli, A., McConochie, J., Ghantous, M., Loffredo, L. and Babanin, A.V., 2012. The effect
823 of wave-induced turbulence on the ocean mixed layer during tropical cyclones: Field
824 observations on the australian north-west shelf. *Journal of Geophysical Research:
825 Oceans*, 117(C11).
- 826 Umlauf, L. and Burchard, H., 2003. A generic length-scale equation for geophysical
827 turbulence models. *Journal of Marine Research*, 61(2): 235-265.
- 828 Warner, J.C., Defne, Z., Haas, K. and Arango, H.G., 2013. A wetting and drying scheme for
829 roms. *Computers & Geosciences*, 58: 54-61.
- 830 Wu, R., Zhang, H. and Chen, D., 2020. Effect of typhoon kalmaegi (2014) on northern south
831 china sea explored using multi-platform satellite and buoy observations data.
832 *Progress in Oceanography*, 180: 102218.
- 833 Xu, J., Chao, S.-Y., Hood, R.R., Wang, H.V. and Boicourt, W.C., 2002. Assimilating high-
834 resolution salinity data into a model of a partially mixed estuary. *Journal of
835 Geophysical Research: Oceans*, 107(C7): 11-1-11-14.
- 836 Xu, Y. and Yu, X., 2021. Enhanced atmospheric wave boundary layer model for evaluation
837 of wind stress over waters of finite depth. *Progress in Oceanography*, 198: 102664.
- 838 Yang, B., Hou, Y., Hu, P., Liu, Z. and Liu, Y., 2015. Shallow ocean response to tropical
839 cyclones observed on the continental shelf of the northwestern south china sea.



- 840 Journal of Geophysical Research: Oceans, 120(5): 3817-3836.
- 841 Zhai, X., Greatbatch, R.J., Eden, C. and Hibiya, T., 2009. On the loss of wind-induced near-
- 842 inertial energy to turbulent mixing in the upper ocean. Journal of Physical
- 843 Oceanography, 39(11): 3040-3045.
- 844 Zhang, F., Li, M. and Miles, T., 2018. Generation of near-inertial currents on the mid-atlantic
- 845 bight by hurricane arthur (2014). Journal of Geophysical Research: Oceans, 123(4):
- 846 3100-3116.
- 847 Zhang, H. et al., 2016. Upper ocean response to typhoon kalmaegi (2014). Journal of
- 848 Geophysical Research: Oceans, 121(8): 6520-6535.
- 849